Draft version February 9, 2015
Preprint typeset using LaTeX style emulateapj v. 5/2/11

arXiv:1410.1535v2 [astro-ph.GA] 6 Feb 2015

THE SIZES OF $Z \sim 6-8$ LENSED GALAXIES FROM THE HUBBLE FRONTIER FIELDS ABELL 2744 DATA

Ryota Kawamata[1], Masafumi Ishigaki[2,3], Kazuhiro Shimasaku[1,4], Masamune Oguri[2,4,5], and Masami Ouchi[3,5]

Draft version February 9, 2015

ABSTRACT

We investigate sizes of $z \sim 6-8$ dropout galaxies using the complete data of the Abell 2744 cluster and parallel fields in the Hubble Frontier Fields program. By directly fitting light profiles of observed galaxies with lensing-distorted Sérsic profiles on the image plane with the `glafic` software, we accurately measure intrinsic sizes of 31 $z \sim 6-7$ and eight $z \sim 8$ galaxies, including those as faint as $M_{\rm UV} \simeq -16.6$. We find that half-light radii $r_{\rm e}$ positively correlates with UV luminosity at each redshift, although the correlation is not very tight. Largest ($r_{\rm e} > 0.8$ kpc) galaxies are mostly red in UV color while smallest ($r_{\rm e} < 0.08$ kpc) ones tend to be blue. We also find that galaxies with multiple cores tend to be brighter. Combined with previous results at $2.5 \lesssim z \lesssim 12$, our result confirms that the average $r_{\rm e}$ of bright ($(0.3-1)L^{\star}_{z=3}$) galaxies scales as $r_{\rm e} \propto (1+z)^{-m}$ with $m = 1.24 \pm 0.1$. We find that the ratio of $r_{\rm e}$ to virial radius is virtually constant at $3.3 \pm 0.1\%$ over a wide redshift range, where the virial radii of hosting dark matter halos are derived based on the abundance matching. This constant ratio is consistent with the disk formation model by Mo et al. (1998) with $j_{\rm d} \sim m_{\rm d}$, where $j_{\rm d}$ and $m_{\rm d}$ are the fractions of the angular momentum and mass within halos confined in the disks. A comparison with various types of local galaxies indicates that our galaxies are most similar to circumnuclear star-forming regions of barred galaxies in the sense that a sizable amount of stars are forming in a very small area.

Subject headings: galaxies: evolution — galaxies: high-redshift — galaxies: photometry — galaxies: structure — gravitational lensing: strong

1. INTRODUCTION

The size of galaxies and its redshift evolution provide fundamental information on the evolution of galactic structure. Size measurements of high-z galaxies are particularly important for understanding the early phase in the formation of galactic disks.

The high resolution of the Hubble Space Telescope (HST) and sensitive cameras installed on it have made it possible to measure the size of high-z galaxies. With the GOODS data from the Advanced Camera for Surveys (ACS), Ferguson et al. (2004) have investigated galaxy sizes over $z \sim 1-5$ to find that the average half-light radius, $r_{\rm e}$, of bright ($\sim L^{\star}_{z=3}$, where $L^{*}_{\rm z=3}$ is the characteristic UV luminosity of $z \sim 3$ LBGs derived in Steidel et al. 1999) galaxies decreases with redshift approximately as $(1+z)^{-m}$ with $m \simeq 1.5$. Bouwens et al. (2004) have also found a similar scaling but with $m \simeq 1$ for $z \sim 2.5-6.0$ galaxies in the Hubble Ultra Deep Field data. These scalings with redshift imply that galaxies at a fixed luminosity evolve in dark matter halos of a constant mass (in the case of $m = 1$) or a constant circular velocity ($m = 1.5$) on the assumption that their half-light radii scale linearly with the virial radii of their hosting dark matter halos, although this non-trivial assumption needs verification.

The decreasing trend of galaxy sizes has been found to continue up to $z \sim 7-12$, with $1 \lesssim m \lesssim 1.5$, by several papers based on deep data including those from the HUDF09 (Beckwith et al. 2006), CANDELS (Koekemoer et al. 2011; Grogin et al. 2011), and HUDF12 (Ellis et al. 2013; Koekemoer et al. 2013) taken with the WFC3/IR camera (e.g. Oesch et al. 2010; Grazian et al. 2012; Ono et al. 2013; Holwerda et al. 2014), although Curtis-Lake et al. (2014) have recently found that the modal value of the log-normal distribution of half-light radii does not significantly evolve over $z \sim 4-8$. In particular, Ono et al. (2013) have accurately measured sizes for nine $z \sim 7$ and six $z \sim 8$ galaxies from the HUDF12 using `GALFIT` (Peng et al. 2002, 2010), to provide the first evidence for continuation of the decreasing trend beyond $z \simeq 8$. They have also found a clear size–luminosity relation at $z \sim 7-8$, which implies that the star formation rate (*SFR*) correlates with the star-formation rate surface density ($\Sigma_{\rm SFR}$).

However, beyond $z \sim 6$, the existing samples of accurate size measurements are not large enough to determine the size–luminosity relation and its tightness. New samples from sky areas other than the current deep fields are needed to improve the statistics and reduce the effect of cosmic variance. The larger sample of size measurements also enables one to extend the analysis by, for example, examining the dependence of the size–luminosity relation on other physical quantities such as galaxy colors.

Besides exploiting the instrumental development, using gravitational lensing (GL) is also effective to probe high-z galaxies. One can investigate detailed properties

Email: kawamata@astron.s.u-tokyo.ac.jp
[1] Department of Astronomy, Graduate School of Science, The University of Tokyo, 7-3-1 Hongo, Bunkyo-ku, Tokyo 113-0033, Japan
[2] Department of Physics, Graduate School of Science, The University of Tokyo, 7-3-1 Hongo, Bunkyo-ku, Tokyo 113-0033, Japan
[3] Institute for Cosmic Ray Research, The University of Tokyo, 5-1-5 Kashiwanoha, Kashiwa, Chiba 277-8582, Japan
[4] Research Center for the Early Universe, The University of Tokyo, 7-3-1 Hongo, Bunkyo-ku, Tokyo 113-0033, Japan
[5] Kavli Institute for the Physics and Mathematics of the Universe (Kavli IPMU, WPI), The University of Tokyo, 5-1-5 Kashiwanoha, Kashiwa, Chiba 277-8583, Japan

of intrinsically faint, high-z galaxies if they are magnified by foreground lens objects. Recent examples of such studies using cluster strong lensing are found in Barone-Nugent et al. (2013) and Alavi et al. (2014).

The Hubble Frontier Fields (HFF; PI: J. Lotz) is an on-going project to observe six high-magnification clusters deeply with the HST. The main purpose of the HFF is to investigate distant faint galaxies in the background of these clusters with help of lensing magnifications. The strong GL effect of these clusters combined with the long exposures enables us to measure sizes for a large number of galaxies as faint as those studied in the HUDF12. Highly magnified, extremely faint (in intrinsic luminosity) galaxies below the HUDF12 detection limit will also be discovered.

In this paper, we study sizes of $z \sim 6-8$ galaxies using the publicly released HFF data of Abell 2744, the first cluster for which the observing program is complete. We measure sizes for 31 galaxies at $z \sim 6-7$ and eight at $z \sim 8$. Combined with the sample from Ono et al. (2013), we now have 40 $z \sim 6-7$ and 14 $z \sim 8$ galaxies with accurate size measurements.

The structure of our paper is as follows. In Section 2, we construct the galaxy sample for this study, and measure intrinsic sizes and luminosities by carefully taking account of the GL effect including the magnification and distortion, as well as correcting for systematic biases inherent in the photometry of faint objects. Results and discussions are given in Section 3. Section 3.1 examines the size–luminosity relation at $z \sim 6-8$. In Section 3.2, we discuss size evolution based on our data and literature data over a wide redshift range. The scaling of galaxy size with the size of hosting dark matter halos is also derived. Section 3.3 compares the state of star formation between $z \sim 6-8$ galaxies and various types of local galaxies in the *SFR*–$\Sigma_{\rm SFR}$ plane. Conclusions are shown in Section 4.

Throughout this paper, we adopt a cosmology with $\Omega_M = 0.3, \Omega_\Lambda = 0.7, H_0 = 70$ km s^{-1} Mpc^{-1}. Magnitudes are given in the AB system (Oke & Gunn 1983). Galaxy sizes are measured in the physical scale. In a companion paper (Ishigaki et al. 2015), we derive the UV luminosity functions of galaxies at $z \sim 5-10$ and discuss their implications for cosmic reionization.

2. SIZE MEASUREMENTS OF $Z \sim 6-8$ GALAXIES

2.1. *Sample Selection*

We measure sizes for a bright subset of i_{814}-dropout and Y_{105}-dropout galaxies in Ishigaki et al. (2015), which are constructed from the version 1.0 release data of Epoch 1 and Epoch 2 of the Abell 2744 main cluster and parallel fields. We use the 30 mas pixel^{-1} image mosaics with the standard correction. For NIR images of the parallel field, the mosaics corrected for time-variable background sky emission are used. See Ishigaki et al. (2015) for details of the sample construction. Briefly, $z \sim 6-7$ galaxies, or i_{814}-dropouts, are selected by:

$$
\begin{aligned}
&i_{814} - Y_{105} > 0.8,\\
&Y_{105} - J_{125} < 0.8,\\
&i_{814} - Y_{105} > 2(Y_{105} - J_{125}) + 0.6,\\
&S/N(Y_{105}) > 5.0, S/N(J_{125}) > 5.0,\\
&S/N(B_{435}) < 2.0, S/N(V_{606}) < 2.0,
\end{aligned}
$$

and $z \sim 8$ galaxies, or Y_{105}-dropouts, are selected by:

$$
\begin{aligned}
&Y_{105} - J_{125} > 0.5,\\
&J_{125} - H_{160} < 0.4,\\
&S/N(J_{125}) > 3.5, S/N(JH_{140}) > 3.5,\\
&S/N(B_{435}) < 2.0, S/N(V_{606}) < 2.0,\\
&S/N(i_{814}) < 2.0.
\end{aligned}
$$

As a result, 18 i_{814}-dropouts and 11 Y_{105}-dropouts are selected in the main cluster field and 17 i_{814}-dropouts and four Y_{105}-dropouts in the parallel field. It is worth noting that most of the Y_{105}-dropouts in the cluster field are highly clustered in a small region. If this overdense region is a forming cluster, they could have some different properties from galaxies in the average field. This overdensity has been reported by some previous studies (e.g. Zheng et al. 2014; Ishigaki et al. 2015).

Galaxy size measurements require high signal-to-noise ratios. To maximize the number of galaxies for size measurements, we coadd the Y_{105}, J_{125}, and JH_{140} images to make a deep UV-continuum image for the size analysis of i_{814}-dropouts, and coadd the J_{125}, JH_{140}, and H_{160} images for Y_{105}-dropouts. In this process, we use `SWarp` (Bertin et al. 2002) and exploit the inverse variance weight images in the release data set, considering differences in exposure time and zero point properly. The 5σ limiting magnitudes of the coadded images are 29.27 ($Y_{105} + J_{125} + JH_{140}$) and 29.10 ($J_{125} + JH_{140} + H_{160}$) for the main cluster field and 29.36 ($Y_{105} + J_{125} + JH_{140}$) and 29.07 ($J_{125} + JH_{140} + H_{160}$) for the parallel field.

We then run `SExtractor` (Bertin & Arnouts 1996) on the coadded images, and select galaxies brighter than the 10σ limiting magnitudes for size measurements. After removing a small number of objects falling in the region of bright intracluster light (ICL) unsuitable for reliable size measurement, we are left with 31 $z \sim 6-7$ galaxies and eight $z \sim 8$ galaxies as given in Tables 1 and 2. One of the $z \sim 6-7$ galaxies is as faint as $M_{\rm UV} \simeq -16.6$ with a high magnification of 11.4, where $M_{\rm UV}$ is the rest-frame UV ($\lambda_{\rm rest} \simeq 1500$ Å) absolute magnitude. This is the faintest $z \gtrsim 6$ galaxy whose size has ever been measured. Ishigaki et al. (2015) have also selected six $z \sim 9$ galaxies, but none of them is included in our analysis because they are either too faint or too close to a bright star.

2.2. *Measurements of Intrinsic Sizes and Luminosities*

To correct for the GL effect on our galaxies, we use the cluster mass map obtained in Ishigaki et al. (2015), in which the mass model is constructed with the pubic software `glafic` (Oguri 2010) using all available multiply lensed objects in the literature plus three newly identified objects. This map is found to be in good agreement with those provided by other research teams which are posted on the public HFF website[7].

While `GALFIT` is widely used for analyzing luminosity profiles of faint galaxies, in this paper we employ `glafic` for size measurements as well, because it enables detailed light profile fitting similar to `GALFIT` for lensed, hence distorted, galaxies. This package finds the best-fit Sérsic profile parameters for a given, lensed galaxy image by

[7] `http://www.stsci.edu/hst/campaigns/frontier-fields/Lensing-Models`

Table 1
Dropout candidates at $z \sim 6-7$ in the Abell 2744 field.

ID	R.A.[a]	Dec[a]	$i_{814}-Y_{105}$	$Y_{105}-J_{125}$	J_{125}[b]	$J_{125}-H_{160}$	Magnification[c,d]	Photo-z	Reference[e]
Cluster field									
HFF1C-i1	3.593804	−30.415447	> 2.37	0.05 ± 0.07	26.10 ± 0.05	$-0.17^{+0.05}_{-0.05}$	$3.73^{+0.24}_{-0.21}$	6.6 ± 0.8	1, 3
HFF1C-i2	3.570654	−30.414659	1.33 ± 0.12	0.11 ± 0.05	26.21 ± 0.03	$-0.08^{+0.06}_{-0.06}$	$1.62^{+0.06}_{-0.06}$	6.0 ± 0.7	1, 3
HFF1C-i3	3.606222	−30.386644	1.07 ± 0.09	0.09 ± 0.04	26.25 ± 0.04	$0.07^{+0.06}_{-0.06}$	$1.69^{+0.05}_{-0.05}$	5.8 ± 0.7	1, 3
HFF1C-i4	3.606385	−30.407282	1.69 ± 0.21	0.00 ± 0.05	26.37 ± 0.04	$-0.33^{+0.07}_{-0.07}$	$2.25^{+0.12}_{-0.10}$	6.3 ± 0.7	1, 3
HFF1C-i5	3.580452	−30.405043	> 2.10	0.17 ± 0.07	26.60 ± 0.05	$-0.22^{+0.09}_{-0.09}$	$5.64^{+0.40}_{-0.39}$	6.8 ± 0.8	1, 3
HFF1C-i6	3.597834	−30.395961	> 1.71	0.27 ± 0.09	26.79 ± 0.07	$-0.27^{+0.10}_{-0.10}$	$2.87^{+0.19}_{-0.19}$	7.0 ± 0.8	1, 3
HFF1C-i7	3.590761	−30.379408	0.95 ± 0.13	-0.16 ± 0.09	27.06 ± 0.08	$-0.13^{+0.12}_{-0.12}$	$1.87^{+0.06}_{-0.05}$	5.9 ± 0.7	···
HFF1C-i9	3.601072	−30.403991	1.11 ± 0.27	0.00 ± 0.11	27.26 ± 0.09	$-0.19^{+0.15}_{-0.15}$	$3.56^{+0.26}_{-0.23}$	5.9 ± 0.7	1, 3
HFF1C-i10	3.600619	−30.410296	> 1.43	-0.06 ± 0.11	27.29 ± 0.08	$-0.45^{+0.18}_{-0.18}$	$11.43^{+1.60}_{-1.20}$	6.4 ± 0.7	3
HFF1C-i11	3.603426	−30.383219	0.87 ± 0.16	-0.13 ± 0.11	27.29 ± 0.09	$-0.15^{+0.15}_{-0.15}$	$1.71^{+0.04}_{-0.05}$	5.8 ± 0.7	3
HFF1C-i12	3.603214	−30.410350	> 1.36	-0.03 ± 0.12	27.32 ± 0.09	$0.10^{+0.14}_{-0.14}$	$3.88^{+0.29}_{-0.21}$	6.3 ± 0.7	1, 2, 3
HFF1C-i13	3.592944	−30.413328	> 1.25	-0.09 ± 0.20	27.35 ± 0.15	$-0.03^{+0.16}_{-0.16}$	$6.85^{+0.60}_{-0.54}$	6.1 ± 0.7	3
HFF1C-i14	3.585016	−30.413084	0.85 ± 0.19	-0.23 ± 0.14	27.45 ± 0.12	$0.14^{+0.16}_{-0.16}$	$2.94^{+0.18}_{-0.17}$	$5.7^{+0.7}_{-1.1}$	···
HFF1C-i15	3.576889	−30.386329	> 0.96	0.13 ± 0.18	27.45 ± 0.16	$-0.27^{+0.19}_{-0.19}$	$2.77^{+0.15}_{-0.13}$	$6.1^{+0.8}_{-0.7}$	3
HFF1C-i16	3.609003	−30.385283	1.35 ± 0.33	-0.07 ± 0.14	27.56 ± 0.12	$-0.12^{+0.19}_{-0.19}$	$1.59^{+0.04}_{-0.04}$	6.1 ± 0.7	3
HFF1C-i17	3.604563	−30.409364	> 0.91	0.12 ± 0.16	27.62 ± 0.11	$-0.25^{+0.22}_{-0.22}$	$2.94^{+0.19}_{-0.16}$	6.1 ± 0.8	3
Parallel field									
HFF1P-i1	3.474802	−30.362578	> 1.80	0.46 ± 0.07	26.52 ± 0.05	$-0.20^{+0.07}_{-0.07}$	1.04	7.3 ± 0.8	···
HFF1P-i2	3.480642	−30.371175	1.76 ± 0.34	-0.02 ± 0.09	26.95 ± 0.07	$-0.45^{+0.11}_{-0.11}$	1.05	6.3 ± 0.7	···
HFF1P-i3	3.487575	−30.364380	1.27 ± 0.33	0.32 ± 0.11	27.06 ± 0.08	$0.08^{+0.10}_{-0.10}$	1.05	5.8 ± 0.7	···
HFF1P-i4	3.488924	−30.394630	> 1.39	0.25 ± 0.11	27.14 ± 0.08	$0.03^{+0.11}_{-0.11}$	1.05	6.7 ± 0.8	···
HFF1P-i5	3.482550	−30.371559	1.19 ± 0.29	0.17 ± 0.11	27.15 ± 0.09	$0.23^{+0.10}_{-0.10}$	1.05	$5.8^{+0.7}_{-1.4}$	···
HFF1P-i6	3.483960	−30.397152	> 1.57	0.00 ± 0.11	27.20 ± 0.09	$-0.07^{+0.12}_{-0.12}$	1.05	6.3 ± 0.7	···
HFF1P-i7	3.467582	−30.396908	> 1.39	0.15 ± 0.12	27.23 ± 0.09	$-0.19^{+0.13}_{-0.13}$	1.04	6.8 ± 0.8	···
HFF1P-i8	3.467097	−30.387686	1.28 ± 0.25	-0.24 ± 0.11	27.30 ± 0.10	$-0.10^{+0.13}_{-0.13}$	1.04	6.0 ± 0.7	···
HFF1P-i9	3.489520	−30.399528	> 1.41	0.05 ± 0.13	27.32 ± 0.10	$-0.26^{+0.14}_{-0.14}$	1.05	6.6 ± 0.8	···
HFF1P-i10	3.466056	−30.394409	1.10 ± 0.30	0.00 ± 0.14	27.43 ± 0.11	$-0.10^{+0.15}_{-0.15}$	1.04	6.0 ± 0.7	···
HFF1P-i11	3.460587	−30.366320	0.92 ± 0.34	0.05 ± 0.18	27.70 ± 0.14	$-0.09^{+0.18}_{-0.18}$	1.04	$5.8^{+0.7}_{-1.1}$	···
HFF1P-i12	3.455844	−30.366359	1.03 ± 0.36	0.00 ± 0.18	27.70 ± 0.14	$0.41^{+0.16}_{-0.16}$	1.03	$4.5^{+1.6}_{-3.9}$	···
HFF1P-i13	3.488139	−30.367864	> 0.91	0.12 ± 0.19	27.73 ± 0.15	$0.01^{+0.18}_{-0.18}$	1.06	$5.8^{+1.0}_{-5.2}$	···
HFF1P-i14	3.486988	−30.399579	0.91 ± 0.33	-0.07 ± 0.18	27.75 ± 0.15	$-0.02^{+0.19}_{-0.19}$	1.05	$5.9^{+0.7}_{-1.1}$	···
HFF1P-i16	3.477238	−30.385998	> 1.02	-0.22 ± 0.21	27.98 ± 0.18	$0.03^{+0.22}_{-0.22}$	1.05	6.5 ± 0.7	···

[a] Coordinates are in J2000.
[b] Total magnitude.
[c] The magnification errors in the parallel field are less than 1%.
[d] Median value of the magnification distribution.
[e] References: (1) Atek et al. (2014b); (2) Zheng et al. (2014); (3) Atek et al. (2014a).

simulating many lensed images with different profile parameters taking account of the GL effect at the position of the galaxy and fitting with them on the observed image. That is, distorted Sérsic profiles are directly compared on the image plane. In this sense, this method is more direct than one in which observed (distorted) images are fit with undistorted profiles created with `GALFIT` and then the best-fit radius and magnitude are corrected for the GL effect simply by dividing by the magnification factor (e.g. Laporte et al. 2014).

In the course of profile fitting, each simulated image is convolved with the PSF when compared with the observed light profile. The PSF profile for each coadded image is determined by stacking four stellar objects in the same image. In case there are nearby foreground galaxies near the target galaxy, we carefully mask these nearby galaxies during the profile fitting.

In this paper, we fix the Sérsic index to $n = 1$, the value widely used in previous studies (e.g. Ono et al. 2013). We use the half-light radius to express galaxy size following previous studies. We have thus six free parameters to determine: positions, half-light radius, flux, ellipticity, and position angle. The upper limit of the ellipticity is set to 0.9. For each galaxy, Sérsic profile fitting is repeated with different initial parameter sets until the best-fit parameters converge. The output fluxes (half-light radii) are converted into absolute magnitudes (radii in physical length) assuming that all the $z \sim 6-7$ and $z \sim 8$ galaxies are located at $z = 6.1$ and $z = 8.0$, respectively.

Some galaxies, e.g., CY-1, appear to consist of multiple components or contain sub-clumps. Although we treat these complex galaxies as single objects, we first fit each system with multiple Sérsic profiles simultaneously in order to obtain reliable sky background estimates for the field. This is because the sky background value obtained

Table 2
Dropout candidates at $z \sim 8$ in the Abell 2744 field.

ID	R.A.[a]	Dec[a]	$Y_{105}-J_{125}$	$J_{125}-H_{160}$	JH_{140}[b]	$JH_{140}-H_{160}$	Magnification[c,d]	Photo-z	Reference[e]
Cluster field									
HFF1C-Y1	3.604518	−30.380467	1.17 ± 0.06	0.04 ± 0.04	25.91 ± 0.02	$0.01^{+0.04}_{-0.04}$	$1.49^{+0.04}_{-0.04}$	8.0 ± 0.9	1, 2, 4, 5, 6
HFF1C-Y2	3.603378	−30.382254	1.26 ± 0.14	0.09 ± 0.07	26.62 ± 0.05	$-0.06^{+0.08}_{-0.08}$	$1.61^{+0.05}_{-0.05}$	8.2 ± 0.9	2, 4, 6
HFF1C-Y3	3.596091	−30.385833	1.30 ± 0.16	-0.00 ± 0.08	26.67 ± 0.05	$-0.07^{+0.08}_{-0.08}$	$2.25^{+0.09}_{-0.09}$	8.2 ± 0.9	2, 4, 6
HFF1C-Y4	3.606461	−30.380996	1.12 ± 0.13	-0.09 ± 0.08	26.94 ± 0.06	$0.08^{+0.10}_{-0.10}$	$1.49^{+0.04}_{-0.04}$	8.0 ± 0.9	2, 4, 6
HFF1C-Y5	3.603859	−30.382263	1.92 ± 0.34	0.35 ± 0.10	26.98 ± 0.07	$0.19^{+0.10}_{-0.10}$	$1.60^{+0.05}_{-0.05}$	8.4 ± 0.9	2, 4, 6
HFF1C-Y6	3.606577	−30.380924	1.09 ± 0.22	0.40 ± 0.12	27.15 ± 0.08	$0.17^{+0.12}_{-0.12}$	$1.48^{+0.04}_{-0.04}$	$7.9^{+0.9}_{-6.1}$	2, 6
Parallel field									
HFF1P-Y1	3.474918	−30.362542	0.61 ± 0.11	0.04 ± 0.08	26.93 ± 0.07	$0.07^{+0.08}_{-0.08}$	1.05	$7.5^{+0.8}_{-1.5}$	···
HFF1P-Y2	3.459245	−30.367360	0.73 ± 0.18	0.02 ± 0.13	27.44 ± 0.11	$0.13^{+0.13}_{-0.13}$	1.04	$7.6^{+0.8}_{-1.7}$	···

[a] Coordinates are in J2000.
[b] Total magnitude.
[c] The magnification errors in the parallel field are less than 1%.
[d] Median value of the magnification distribution.
[e] References: (1) Atek et al. (2014b); (2) Zheng et al. (2014); (3) Zheng et al. (2014) possible candidates; (4) Coe et al. (2014); (5) Laporte et al. (2014); (6) Atek et al. (2014a).

by this multi-component fitting is more stable and robust than single profile fitting of these complex systems. We then perform single profile fitting with the fixed sky background value derived above. Results of light profile fitting for all the dropout galaxies are shown in Figures 9–14 in the Appendix.

There are four very small ($r_e < 0.08$ kpc) galaxies at $z \sim 6-7$: C-i10, C-i13, C-i15, and C-i17. However, we find only one (C-i10) to be actually resolved and calculate for the remaining three an upper limit to the half-light radius, from the examination below: For each object, we replace the real image with a stellar image and conduct a profile fitting in the same manner as for the real object considering the GL effect. This stellar image is taken from the same field without any luminosity correction. We repeat this five times using five different stellar images. Then, if the average of the five output half-light radii is significantly smaller than the half-light radius of the real image, we consider this galaxy to be resolved. If not, we consider it to be unresolved and adopt the average stellar half-light radius for the upper limit. We also confirm that C-i16 is resolved.

We note that C-i5 and C-i6 are lensed images of the same galaxy. We adopt the average values of these two images for the parameters of this galaxy.

2.3. *Error Estimates*

There are three main sources of errors in our size and magnitude measurements: Statistical and systematic errors in light profile fitting, internal statistical errors in lensing magnification and distortion of our mass map, and external systematic errors in lensing effects coming from different assumptions made in creating mass maps. In the HFF project, the last source of errors can be estimated by comparing lensing properties of eight public mass maps that are constructed independently (Ishigaki et al. 2015). These mass maps enable us to discuss the validity of our mass map and to estimate systematic errors caused by differences in the method of mass map construction.

The largest among the three is the error in light profile fitting. It is well known that the size and brightness of very faint galaxies such as those in our sample tend to be biased depending on their size and magnitude even when they are measured from careful profile fitting. For each galaxy, we correct for these systematic errors with the following Monte Carlo approach. (1) We generate a model galaxy image by randomly changing Sérsic parameter values around the best-fit values, and put it randomly near the observed position of the galaxy if it is in the main cluster field, where the GL effect varies from position to position, or randomly in the entire image if it is in the parallel field, where the GL effect is small and nearly constant. In this process, we do not change the GL effect, which depends on its position, because the purpose here is to estimate only photometric errors. (2) We measure its size and magnitude in exactly the same manner as for the observed galaxy. (3) We repeat (1) and (2) to make a table of 100–300 input and measured sizes and magnitudes. (4) From (3), we extract input half-light radii whose measured radii and magnitudes are virtually equal to that of the observed galaxy to create their histogram. The median and the standard deviation of the histogram are adopted as the true radius and its error of the galaxy, respectively. Its true magnitude and error are determined in a similar manner. As an example, the results of the simulations for C-Y1 (the most precise case) and P-i16 (the least precise case) are shown in Figure 1.

Errors in the mass map affect size and magnitude measurements primarily through changes in magnification. Ishigaki et al. (2015) have found that the change in magnification due to the internal errors in our mass map is negligibly small, $\sim 5\%$, for the main cluster field and less than 1% for the parallel field, as given in Tables 3 and 4.

On the other hand, there is a significant variation in magnification among the eight public mass maps (see Figure 11 of Ishigaki et al. 2015). We estimate this systematic error at the position of each dropout by calculating the standard deviation of the eight magnification values excluding the highest and lowest ones. The errors obtained are shown in Tables 3 and 4. The error bars

Table 3
Fitting results for dropouts at $z \sim 6-7$.

ID[a]	$m_{\rm UV}^{\rm AUTO}$[b] [mag]	n	$m_{\rm UV}$[c] [mag]	$M_{\rm UV}$ [mag]	$r_{\rm e}$[d] [kpc]	e	Magnification[e,f]
Cluster field							
HFF1C-i1	26.20 ± 0.01	1.0	$27.68^{+0.04}_{-0.05}$	$-19.05^{+0.04}_{-0.05}$	$0.16^{+0.02}_{-0.02}$	0.31	$3.73^{+0.24+0.65}_{-0.21-0.55}$
HFF1C-i2	26.23 ± 0.01	1.0	$26.79^{+0.04}_{-0.05}$	$-19.93^{+0.04}_{-0.05}$	$0.15^{+0.03}_{-0.03}$	0.90	$1.62^{+0.06+0.15}_{-0.06-0.14}$
HFF1C-i3	26.34 ± 0.01	1.0	$26.76^{+0.04}_{-0.05}$	$-19.96^{+0.04}_{-0.05}$	$0.41^{+0.02}_{-0.02}$	0.19	$1.69^{+0.05+0.33}_{-0.05-0.18}$
HFF1C-i4	26.75 ± 0.02	1.0	$27.45^{+0.04}_{-0.05}$	$-19.27^{+0.04}_{-0.05}$	$0.14^{+0.02}_{-0.02}$	0.37	$2.25^{+0.12+1.01}_{-0.10-0.18}$
HFF1C-i5	26.71 ± 0.02	1.0	$28.71^{+0.06}_{-0.06}$	$-18.01^{+0.06}_{-0.06}$	$0.14^{+0.02}_{-0.02}$	0.42	$5.64^{+0.40+0.11}_{-0.39-0.69}$
HFF1C-i6	27.06 ± 0.02	1.0	$28.25^{+0.08}_{-0.07}$	$-18.47^{+0.08}_{-0.07}$	$0.09^{+0.02}_{-0.03}$	0.65	$2.87^{+0.19+0.73}_{-0.19-0.09}$
*HFF1C-i7	26.40 ± 0.01	1.0	$27.13^{+0.09}_{-0.15}$	$-19.59^{+0.09}_{-0.15}$	$0.73^{+0.10}_{-0.07}$	0.65	$1.87^{+0.06+0.80}_{-0.05-0.07}$
*HFF1C-i9	27.14 ± 0.02	1.0	$28.00^{+0.10}_{-0.17}$	$-18.72^{+0.10}_{-0.17}$	$0.55^{+0.07}_{-0.06}$	0.54	$3.56^{+0.26+0.58}_{-0.23-0.43}$
HFF1C-i10	27.83 ± 0.04	1.0	$30.07^{+0.09}_{-0.09}$	$-16.65^{+0.09}_{-0.09}$	$0.03^{+0.01}_{-0.01}$	0.85	$11.4^{+1.60+0.06}_{-1.20-2.55}$
HFF1C-i11	27.71 ± 0.04	1.0	$28.00^{+0.08}_{-0.07}$	$-18.72^{+0.08}_{-0.07}$	$0.15^{+0.03}_{-0.04}$	0.40	$1.71^{+0.04+0.46}_{-0.05-0.24}$
HFF1C-i12	26.44 ± 0.01	1.0	$27.91^{+0.11}_{-0.11}$	$-18.81^{+0.11}_{-0.11}$	$0.57^{+0.05}_{-0.06}$	0.47	$3.88^{+0.29+5.12}_{-0.21-0.26}$
HFF1C-i13	27.69 ± 0.04	1.0	$29.58^{+0.06}_{-0.07}$	$-17.14^{+0.06}_{-0.07}$	< 0.04	0.78	$6.85^{+0.60+1.65}_{-0.54-1.31}$
HFF1C-i14	26.65 ± 0.01	1.0	$28.53^{+0.12}_{-0.14}$	$-18.19^{+0.12}_{-0.14}$	$0.23^{+0.07}_{-0.07}$	0.51	$2.94^{+0.18+0.56}_{-0.17-0.16}$
HFF1C-i15	27.61 ± 0.03	1.0	$28.96^{+0.09}_{-0.11}$	$-17.76^{+0.09}_{-0.11}$	< 0.06	0.85	$2.77^{+0.15+4.65}_{-0.13-0.00}$
HFF1C-i16	27.82 ± 0.04	1.0	$28.37^{+0.09}_{-0.19}$	$-18.35^{+0.09}_{-0.19}$	$0.08^{+0.04}_{-0.04}$	0.90	$1.59^{+0.04+0.61}_{-0.04-0.16}$
HFF1C-i17	27.89 ± 0.04	1.0	$29.19^{+0.09}_{-0.11}$	$-17.53^{+0.09}_{-0.11}$	< 0.08	0.89	$2.94^{+0.19+3.70}_{-0.16-0.23}$
Parallel field							
*HFF1P-i1	26.36 ± 0.01	1.0	$26.75^{+0.05}_{-0.07}$	$-19.97^{+0.05}_{-0.07}$	$0.52^{+0.05}_{-0.06}$	0.68	1.04
HFF1P-i2	27.28 ± 0.03	1.0	$27.20^{+0.08}_{-0.07}$	$-19.52^{+0.08}_{-0.07}$	$0.40^{+0.04}_{-0.05}$	0.42	1.05
HFF1P-i3	26.87 ± 0.02	1.0	$26.92^{+0.10}_{-0.10}$	$-19.80^{+0.10}_{-0.10}$	$0.83^{+0.09}_{-0.07}$	0.27	1.05
HFF1P-i4	26.91 ± 0.02	1.0	$27.35^{+0.12}_{-0.11}$	$-19.37^{+0.12}_{-0.11}$	$0.60^{+0.07}_{-0.10}$	0.55	1.05
HFF1P-i5	27.43 ± 0.03	1.0	$27.19^{+0.09}_{-0.09}$	$-19.53^{+0.09}_{-0.09}$	$0.64^{+0.07}_{-0.06}$	0.21	1.05
HFF1P-i6	27.04 ± 0.02	1.0	$27.21^{+0.11}_{-0.11}$	$-19.51^{+0.11}_{-0.11}$	$0.60^{+0.09}_{-0.11}$	0.70	1.05
HFF1P-i7	27.23 ± 0.02	1.0	$27.06^{+0.12}_{-0.12}$	$-19.66^{+0.12}_{-0.12}$	$0.81^{+0.08}_{-0.10}$	0.50	1.04
HFF1P-i8	27.34 ± 0.03	1.0	$27.26^{+0.10}_{-0.10}$	$-19.46^{+0.10}_{-0.10}$	$0.56^{+0.07}_{-0.08}$	0.44	1.04
HFF1P-i9	27.37 ± 0.03	1.0	$27.54^{+0.11}_{-0.12}$	$-19.18^{+0.11}_{-0.12}$	$0.41^{+0.08}_{-0.09}$	0.57	1.05
HFF1P-i10	27.70 ± 0.04	1.0	$27.45^{+0.12}_{-0.14}$	$-19.27^{+0.12}_{-0.14}$	$0.45^{+0.10}_{-0.11}$	0.74	1.04
HFF1P-i11	26.80 ± 0.02	1.0	$28.35^{+0.12}_{-0.10}$	$-18.37^{+0.12}_{-0.10}$	$0.12^{+0.07}_{-0.05}$	0.90	1.04
HFF1P-i12	27.62 ± 0.03	1.0	$27.58^{+0.23}_{-0.18}$	$-19.14^{+0.23}_{-0.18}$	$0.80^{+0.13}_{-0.18}$	0.45	1.03
HFF1P-i13	27.45 ± 0.03	1.0	$27.39^{+0.20}_{-0.18}$	$-19.33^{+0.20}_{-0.18}$	$1.04^{+0.18}_{-0.17}$	0.31	1.06
HFF1P-i14	27.67 ± 0.04	1.0	$27.22^{+0.15}_{-0.16}$	$-19.50^{+0.15}_{-0.16}$	$1.00^{+0.16}_{-0.14}$	0.26	1.05
HFF1P-i16	27.83 ± 0.04	1.0	$28.07^{+0.17}_{-0.19}$	$-18.65^{+0.17}_{-0.19}$	$0.34^{+0.14}_{-0.13}$	0.90	1.05

[a] Asterisks indicate galaxies with multiple cores.
[b] `MAG_AUTO` magnitude from `SExtractor`.
[c] Total apparent magnitude from light profile fitting with `glafic`.
[d] Circularized effective radius, $r_{\rm e}^{\rm maj}\sqrt{1-e}$, where $r_{\rm e}^{\rm maj}$ is the radius along the major axis and e the ellipticity.
[e] Best fitted value of magnification.
[f] The first error shows the error in our mass map, and the second error shows the variation in magnification among the other eight public mass maps.

plotted in Figure 2 are a quadratic sum of this systematic error and the error in profile fitting.

The best-fit values and errors for all the dropout galaxies are summarized in Tables 3 and 4.

3. RESULTS AND DISCUSSION

3.1. *Size–luminosity relation*

Figure 2 shows the distribution of our galaxies in the $r_{\rm e}$–$M_{\rm UV}$ plane for the two redshift ranges. Also plotted are the galaxies selected in Ono et al. (2013) who investigated the size distribution of HUDF12 galaxies over similar redshift ranges using `GALFIT`. Because of the difference in the dropout band (i_{814} vs z_{850}), the redshift distribution of our $z \sim 6-7$ galaxies is somewhat different from that of the HUDF12 galaxies which are distributed around $z \approx 7$ (Figure 3). However, since there seems to be little size evolution between $z \sim 6$ and $z \sim 7$ (see Figure 6), we merge these two samples into one to improve the statistics.

The merged sample is less affected by cosmic variance than the HUDF12 sample. Calculation based on Robertson et al. (2014) finds that at $z \sim 7$ the cosmic variance in the number density of $M_{\rm UV} = -20$ galaxies reduces from 50% from 30% by adding our sample to the HUDF12 one. Similarly, a reduction from 60% to 40% is expected at $z \sim 8$.

Similar to Ono et al. (2013), we find a positive correlation between half-light radius and luminosity in our sample for both redshift ranges. The average size of our galaxies as a function of luminosity is also in a rough

Table 4
Fitting results for dropouts at $z \sim 8$.

ID[a]	$m_{\rm UV}^{\rm AUTO}$[b] [mag]	n	$m_{\rm UV}$[c] [mag]	$M_{\rm UV}$ [mag]	$r_{\rm e}$[d] [kpc]	e	Magnification[e,f]
Cluster field							
*HFF1C-Y1	25.97 ± 0.02	1.0	$26.20^{+0.03}_{-0.03}$	$-20.95^{+0.03}_{-0.03}$	$0.24^{+0.02}_{-0.02}$	0.70	$1.49^{+0.04+0.56}_{-0.04-0.11}$
*HFF1C-Y2	25.99 ± 0.02	1.0	$26.48^{+0.05}_{-0.13}$	$-20.67^{+0.05}_{-0.13}$	$0.62^{+0.05}_{-0.05}$	0.60	$1.61^{+0.05+0.55}_{-0.05-0.17}$
HFF1C-Y3	26.58 ± 0.03	1.0	$27.13^{+0.06}_{-0.10}$	$-20.01^{+0.06}_{-0.10}$	$0.38^{+0.03}_{-0.03}$	0.20	$2.25^{+0.09+3.06}_{-0.09-0.26}$
HFF1C-Y4	26.66 ± 0.03	1.0	$27.27^{+0.09}_{-0.12}$	$-19.88^{+0.09}_{-0.12}$	$0.27^{+0.06}_{-0.05}$	0.65	$1.49^{+0.04+0.62}_{-0.04-0.11}$
*HFF1C-Y5	26.16 ± 0.02	1.0	$26.61^{+0.10}_{-0.13}$	$-20.54^{+0.10}_{-0.13}$	$0.84^{+0.08}_{-0.09}$	0.46	$1.60^{+0.05+0.54}_{-0.05-0.17}$
HFF1C-Y6	26.46 ± 0.02	1.0	$26.59^{+0.15}_{-0.20}$	$-20.55^{+0.15}_{-0.20}$	$0.92^{+0.14}_{-0.10}$	0.44	$1.48^{+0.04+0.63}_{-0.04-0.11}$
Parallel field							
*HFF1P-Y1	27.15 ± 0.03	1.0	$27.14^{+0.09}_{-0.09}$	$-20.00^{+0.09}_{-0.09}$	$0.24^{+0.05}_{-0.07}$	0.65	1.05
HFF1P-Y2	27.07 ± 0.03	1.0	$27.48^{+0.11}_{-0.14}$	$-19.66^{+0.11}_{-0.14}$	$0.21^{+0.07}_{-0.07}$	0.90	1.04

[a] Asterisks indicate galaxies with multiple cores.
[b] `MAG_AUTO` magnitude from `SExtractor`.
[c] Total apparent magnitude from light profile fitting with `glafic`.
[d] Circularized effective radius, $r_{\rm e}^{\rm maj}\sqrt{1-e}$, where $r_{\rm e}^{\rm maj}$ is the radius along the major axis and e the ellipticity.
[e] Best fitted value of magnification.
[f] The first error shows the error in our mass map, and the second error shows the variation in magnification among the other eight public mass maps.

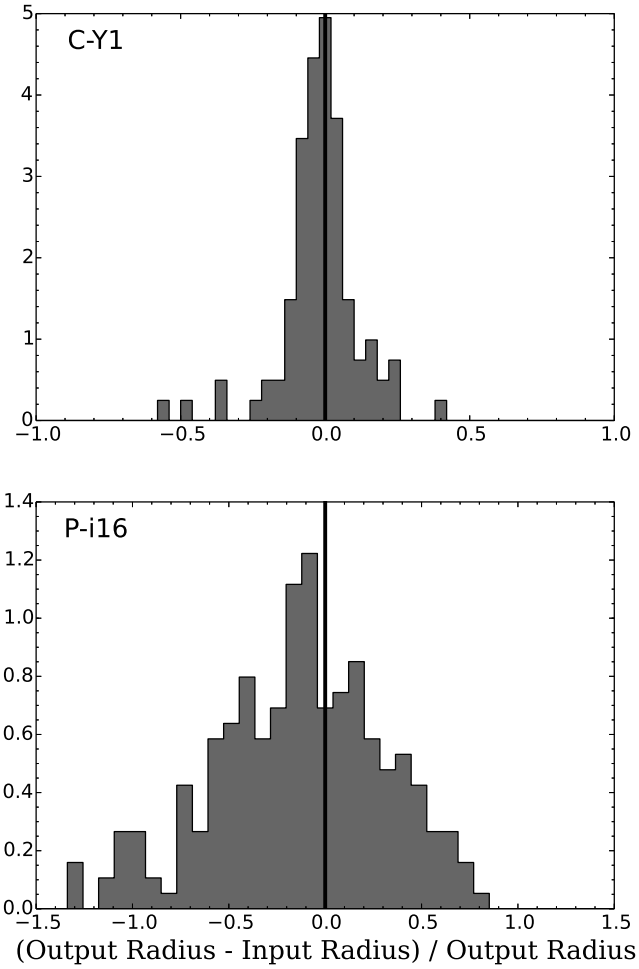

Figure 1. Examples of the simulations to estimate the error in half-light radius. The upper and lower panels show the normalized distribution of the difference between input and measured radii for C-Y1 and P-i16, respectively.

agreement with the result of Ono et al. (2013), once the statistical uncertainties are taken into account. However, at both redshift ranges, the correlation seen in our sample is much weaker than that of Ono et al. (2013). For example, around $M_{\rm UV} \sim -19$ to -20, the sizes of our $z \sim 6-7$ galaxies are distributed over 0.1 kpc – 1.0 kpc. This is perhaps a consequence of the much larger sample size and less cosmic variance of our sample as compared with the sample of Ono et al. (2013).

Huang et al. (2013) have also found a large scatter in size for dropout galaxies at $z \sim 4$ and 5. A relatively weak correlation between size and luminosity may be common at high redshifts.

Our sample contains two very bright and compact galaxies, C-Y1 at $z \sim 8$ and C-i2 at $z \sim 6-7$. Both galaxies have also been identified in previous papers analyzing the HFF data. C-Y1 has been reported by Laporte et al. (2014) to have $r_{\rm e} = 0.35 \pm 0.15$ kpc and $M_{\rm UV} = -20.88 \pm 0.04$, consistent with our measurements. C-i2 has been identified by Atek et al. (2014b) with $M_{\rm UV} = -20.45 \pm 0.03$, also consistent with our value.

There is no faint and large galaxy found in our sample. At $z \sim 8$, it is unlikely that we are missing a significant fraction of such galaxies due to selection bias, because our galaxies are distributed in the $r_{\rm e}$–$M_{\rm UV}$ plane well separate from the boundary of 50% detection completeness shown by the dashed and dash-dot lines. However, since some of our galaxies at $z \sim 6-7$ are close to the completeness lines, their size distribution can be affected by the completeness effect. These completeness lines are determined by the following process. (1) We generate model galaxies over wide magnitude and size ranges and put them randomly on the detection image. (2) We run `SExtractor` on this image in exactly the same manner as for the original image. (3) The detection rate is found to decrease with increasing size. The size at which the detection rate is 50% is obtained as a function of absolute magnitude.

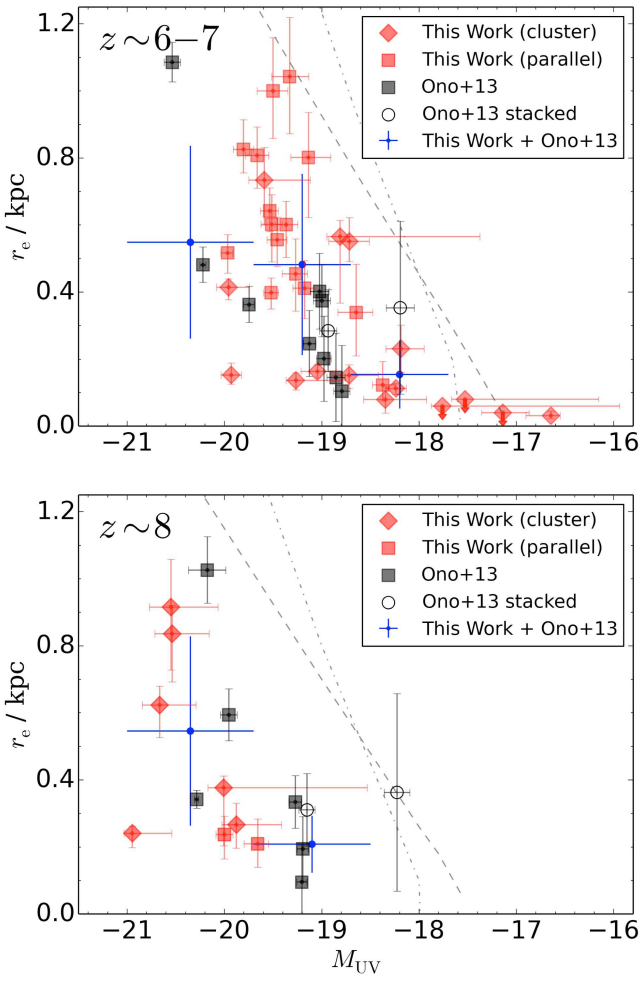

Figure 2. Size–luminosity relation for $z \sim 6-7$ (top) and $z \sim 8$ (bottom) galaxies. The red and gray points represent our galaxies and Ono et al. (2013)'s, respectively. Rhombuses represent galaxies from the cluster field and squares from the parallel and blank fields. Arrows represent galaxies whose half-light radius is an upper limit. The error bars of our galaxies show conservative errors that include the fitting error and the variation in magnification among the eight other mass maps. The blue points with bars indicate the average size and the scatter in the given luminosity bin for the merged sample of this study and Ono et al. (2013). The dashed and dash-dot lines indicate the 50% completeness lines for our samples in the cluster and parallel fields, respectively.

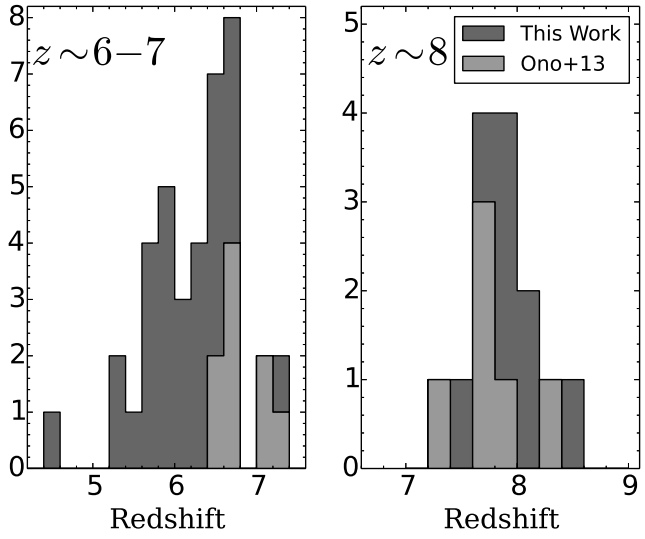

Figure 3. Redshift distribution for $z \sim 6-7$ (left) and $z \sim 8$ (right) galaxies. The gray and light gray histograms represent our galaxies and Ono et al. (2013)'s, respectively.

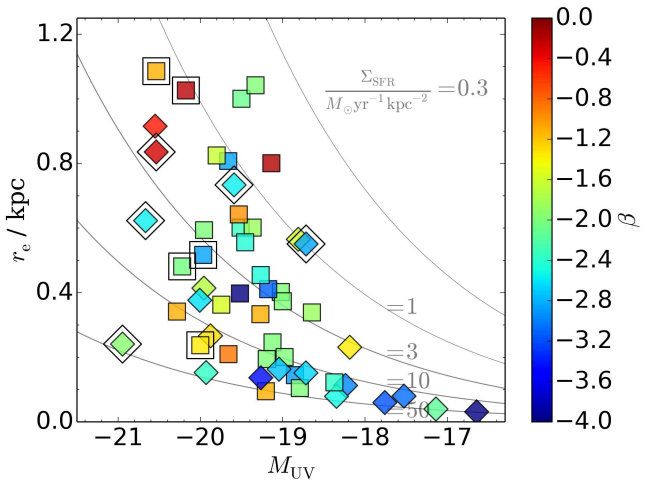

Figure 4. Size–luminosity relation for the merged sample of $z \sim 6-8$. Rhombuses represent galaxies from the cluster field and squares from the parallel and blank fields. Galaxies are color-coded by the UV power-law index, β. The solid lines correspond to constant star formation surface densities of $\Sigma_{SFR}/(M_\odot yr^{-1}kpc^{-2}) = 0.3, 1, 3, 10, 50$. Galaxies with multiple cores are marked by a large, open rhombus or square.

The blue points with error bars in each panel of Figure 2 indicate the average size and the scatter in the given luminosity bin for the merged sample of this study and Ono et al. (2013). The average correlations at two redshifts agree well with each other, indicating that the size–luminosity relation does not significantly evolve from $z \sim 6-7$ to ~ 8. Therefore, we combine the two redshift ranges together to examine the dependence of the size–luminosity relation on two other galaxy properties, UV color and multiplicity.

UV color. Figure 4 plots half-light radii against UV luminosities for all the galaxies in the combined sample, colored according to the UV slope β that is defined as $f_\lambda \propto \lambda^\beta$ with f_λ being the UV continuum flux density with respect to wavelength λ. We calculate β using the equations given in Bouwens et al. (2013): $\beta = -2.0 + 4.39(J_{125} - H_{160})$ for $z \sim 6-7$ and $\beta = -2.0 + 8.98(JH_{140} - H_{160})$ for $z \sim 8$. For each redshift, the range of β in our sample is consistent with those of Bouwens et al. (2013) and Dunlop et al. (2013).

We find that largest (> 0.8 kpc) galaxies tend to be bright ($M_{UV} \lesssim -19.5$) while the remaining galaxies have a wide range of luminosity with a weak correlation with size, as already seen in each panel of Figure 2 with smaller statistics. We also find that largest (> 0.8 kpc) galaxies are mostly red and smallest (< 0.08 kpc) galaxies are mostly blue, while the remainings do not show a very strong trend. There are mainly three factors that make galaxies red: high dust extinction, old age, and high metallicity. Since these three characteristics are often seen in evolved galaxies, selecting largest galaxies may lead to effectively picking out evolved galaxies at the redshifts studied here.

We note that the faintest galaxy in the sample, C-

i10, with $M_{\rm UV} = -16.6$, is also the bluest ($\beta = -4.00$) and smallest ($r_{\rm e} = 0.03$ kpc) object. This interesting galaxy, detected thanks to the high lensing magnification of $\mu \simeq 11$, may be a very young galaxy with an extremely low metallicity. This galaxy has also been reported by Atek et al. (2014a) to have $M_{\rm UV} = -15.80 \pm 0.16$.

Multiplicity. We also examine if galaxies with multiple cores have any preference in size or luminosity. Multiple cores can be regarded as a sign of a recent merging event. Many papers have estimated the fraction of galaxies with multiple cores at high redshift (e.g. Ravindranath et al. 2006; Lotz et al. 2008; Oesch et al. 2010; Law et al. 2012; Guo et al. 2012; Jiang et al. 2013). For example, Ravindranath et al. (2006) have reported that 30% of $z \sim 3$ LBGs have multiple cores, and Jiang et al. (2013) have found that $40\% - 50\%$ of bright ($M_{\rm UV} \leq -20.5$) galaxies at $5.7 \leq z \leq 7.0$ have multiple cores.

We identify galaxies with multiple cores in our sample by visual inspection, considering the claim by Jiang et al. (2013) that while galaxies at $z \gtrsim 6$ are too small and faint for quantitative morphological analysis, visual inspection is still valid for examining whether or not a galaxy has multiple cores. Galaxies with multiple cores are marked with a large square in Figure 4, and marked with a star in Figures 9–14. Ten galaxies, or 19% of the sample, are found to have multiple cores. This fraction is similar to that derived by Oesch et al. (2010) at similar redshifts. As seen in the galaxy images summarized in Appendix, for most of the galaxies with multiple cores, the primary cores are distinct compared to the secondary or later cores, which perhaps implies relatively minor mergers.

As can be seen from Figure 4, most of the galaxies with multiple cores are bright ($M_{\rm UV} \lesssim -20$), qualitatively consistent with the trend seen in the sample of Oesch et al. (2010) that brighter galaxies tend to have multiple cores. More specifically, in the sample of Oesch et al. (2010), the brightest and fourth brightest galaxies have multiple cores among the 16 $z \sim 7$ galaxies. In our sample, three of the four brightest galaxies ($M_{\rm UV} \leq -20.5$) at $z \sim 8$ have multiple cores. On the other hand, we find that the sizes of galaxies with multiple cores are distributed widely from 0.2 kpc to 1 kpc.

At $z \sim 6 - 7$, the bright galaxies ($-20 \leq M_{\rm UV} \leq -19.0$) from the cluster field are on average smaller than those from the parallel field. We find about a factor of two difference in the average size of those galaxies (0.32 ± 0.23 kpc for the cluster field and 0.67 ± 0.20 kpc for the parallel field). This discrepancy might be caused by sample variance and/or cosmic variance.

3.2. *Redshift evolution of size*

Figure 5 shows the average half-light radius as a function of UV luminosity for $2.5 \leq z \lesssim 9 - 10$ LBGs and for $z \sim 0$ spirals and $z \sim 0.5$ irregulars for comparison. Galaxies from our merged sample are plotted as orange ($z \sim 6 - 7$) and red ($z \sim 8$) filled circles. Huang et al. (2013), Jiang et al. (2013), Ono et al. (2013), and Holwerda et al. (2014) have used `GALFIT` to measure sizes and luminosities, while Bouwens et al. (2004) have used half-light radii based on Kron-style magnitudes, and Oesch et al. (2010) and Grazian et al. (2012) based on `SExtractor`.

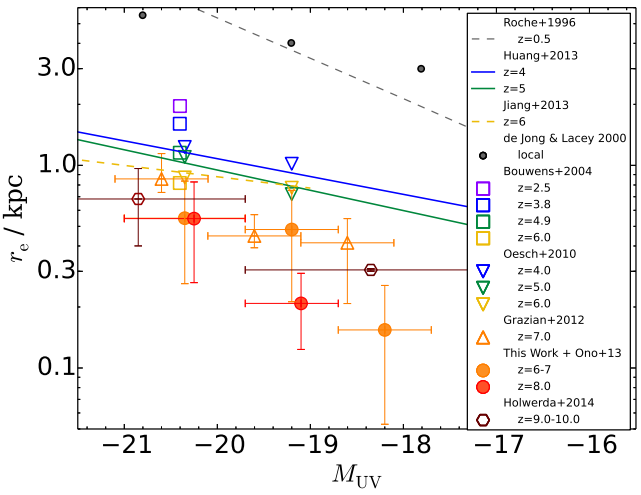

Figure 5. Size–luminosity relations for $2.5 \leq z \lesssim 9 - 10$ LBGs, overplotted with those for local spiral galaxies and $z \sim 0.5$ irregular galaxies. Our samples combined with Ono et al. (2013)'s are shown by orange ($z \sim 6$–7) and red ($z \sim 8$) filled circles. The purple, blue, green, and yellow open squares are for $z \sim 2.5$, $z \sim 3.8$, $z \sim 4.9$, and $z \sim 6$ LBGs by Bouwens et al. (2004); the blue, green, and yellow open inverse triangles for $z \sim 4$, $z \sim 5$, and $z \sim 6$ LBGs by Oesch et al. (2010); the orange triangles for $z \sim 7$ LBGs by Grazian et al. (2012); and the brown open hexagons for $z \sim 9 - 10$ LBGs by Holwerda et al. (2014). The blue and green lines show the average relations for LBGs at $z \sim 4$ and $z \sim 5$ by Huang et al. (2013), and the yellow dashed line the average relation for Lyα emitters and LBGs at $z \sim 5.7 - 6.5$ by Jiang et al. (2013). The black dots represent the average relation for local spiral galaxies by de Jong & Lacey (2000) and the black dotted line is for $z \sim 0.5$ irregular galaxies by Roche et al. (1996). The error bars in $r_{\rm e}$ are the 1σ standard deviations while those in $M_{\rm UV}$ correspond to the bin widths.

From this figure, we find that the average size around $M_{\rm UV} = -20.4$ gradually becomes smaller with redshift from $z \sim 2.5$ to $z \sim 7$ but the evolution from $z \sim 7$ to $z \sim 9 - 10$ is not significant. The slopes of the size–luminosity relation for $z \sim 6 - 8$ galaxies seem to be steeper than those for $z \sim 4 - 5$ galaxies, although the statistical uncertainty is still large. This may indicate that fainter, or less massive, galaxies grow in size more rapidly over $z \sim 4 - 8$. It is worth noting that among the two local ($z \lesssim 0.5$) galaxy populations, irregular galaxies have a steep slope similarly to those of $z \sim 6 - 8$ galaxies.

Plotted in Figure 6 is the average half-light radius of bright ($(0.3 - 1)L^*_{\rm z=3}$) galaxies as a function of redshift. In the calculation of the average radii for the merged samples of this work and Ono et al. (2013), we reduce the weight of the samples from the cluster field according to the uncertainty in the mass model. For the cluster-field sample at each redshift, the uncertainty in magnification is calculated from the average of the variances in magnification among the eight public mass maps at the positions of the sample galaxies. This uncertainty is then converted into the uncertainty in radius and is quadratically added to the statistical error in the average radius for this sample, thus resulting in a reduction of the weight compared with the parallel-field and Ono et al. (2013)'s samples for which only the statistical error is considered. We include the $z \sim 12$ object given in Ono et al. (2013). The data of Ferguson et al. (2004) are not included because their sample includes brighter ($< 5L^*_{\rm z=3}$) galaxies. We find that the average size of bright galaxies decreases from $z \sim 2.5$ to $6 - 7$, in agreement with previous results

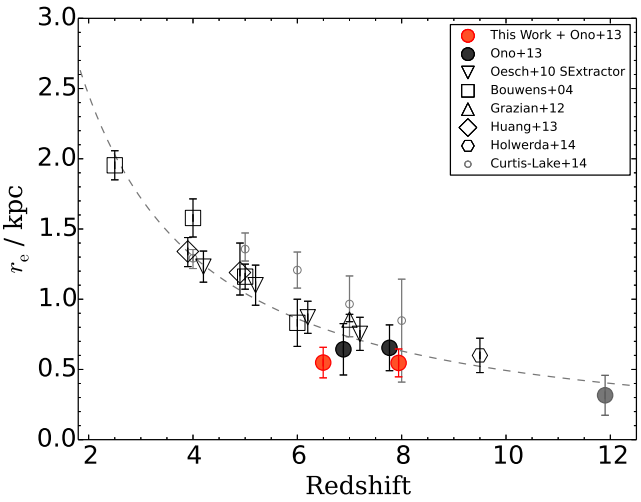

Figure 6. Redshift evolution of the average size of bright galaxies. The red circles show the weighted-average radii of our samples combined with Ono et al. (2013)'s, while the black circles are for Ono et al. (2013)'s. The error bars show the 1σ standard error.

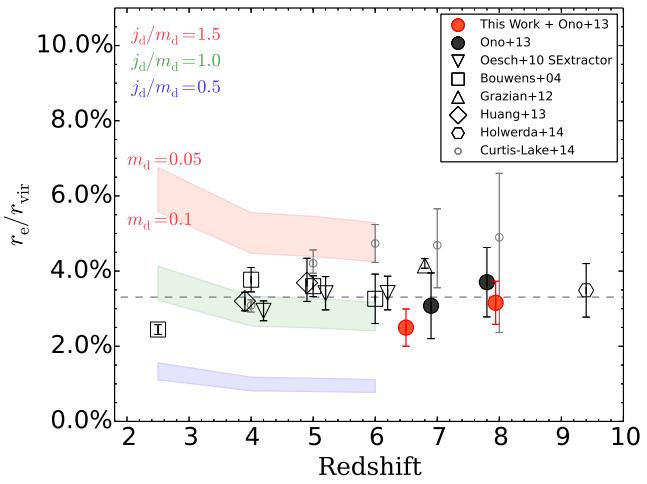

Figure 7. Redshift evolution of the half-light radius to virial radius ratio. The error bars show the 1σ standard error of the half-light radius. The shaded bands are predictions from the model by Mo et al. (1998) changing the j_d/m_d and m_d within the range of $0.05-0.1$. The red, green, and blue bands correspond to $j_d/m_d = 1.5, 1.0, 0.5$. The upper edge of each band corresponds to $m_d = 0.05$ and the lower to $m_d = 0.1$.

(e.g. Bouwens et al. 2004; Hathi et al. 2008; Oesch et al. 2010; Grazian et al. 2012; Huang et al. 2013; Ono et al. 2013), while the evolution between $z \sim 6-7$ and ~ 8 is insignificant. We note that the average radius of our $z \sim 6-7$ combined sample may be underestimated because all but one are in the range of $(0.3-0.5)L^*_{z=3}$.

The small open circles in Fig. 6 indicate the mode of the log-normal distribution of r_e for $z \sim 4-8$ LBGs over the same luminosity range obtained by Curtis-Lake et al. (2014), who have adopted a non-parametric, curve-of-growth method to measure sizes. Their values are slightly but systematically higher than the other measurements except for $z \sim 4$, leading them to conclude that the typical galaxy size does not significantly evolve over $z \sim 4-8$. The reason for this systematic difference is not clear, although we find in our $z \sim 6-7$ sample that adopting the mode instead of the average results in 0.15 kpc *decrease*. Our $z \sim 8$ sample is too small to calculate a modal value.

Fitting the size evolution of $r_e \propto (1+z)^{-m}$ to the data except those of Curtis-Lake et al. (2014) who adopted the modal values gives $m = 1.24 \pm 0.1$, which is consistent with previous results based on average r_e measurements (Oesch et al. 2010; Ono et al. 2013). Analytic models of dark-halo evolution predict that the virial radius scales with redshift as $(1+z)^{-1}$ for halos with a fixed mass and as $(1+z)^{-1.5}$ for halos with a fixed circular velocity (e.g. Ferguson et al. 2004). The value we find, $m = 1.24$, is in the middle of these two cases. However, any previous attempts to link galaxies to dark matter halos using an observed redshift scaling of half-light radius have implicitly made a non-trivial assumption that half-light radius linearly scales with virial radius.

In order to obtain further insights into disk evolution in dark matter halos, we take a different approach. We combine the so-called abundance matching analysis that connects the stellar mass and halo mass with the observed relation between stellar mass and luminosity. Specifically, we adopt the abundance matching result of Behroozi et al. (2013), and the observed stellar mass–luminosity relations of Reddy & Steidel (2009) for $z \sim 2.5$ galaxies and González et al. (2011) for $z \sim 4-7$ galaxies [8] to calculate the halo mass of galaxies in Figure 6 from their UV luminosity. The estimated halo mass of $M_{UV} = -20.2$ galaxies at $z = 6.0$ is $\log(M_h/M_\odot) = 11.2$, in good accordance with the recent clustering result, $\log(M_h/M_\odot) = 11.0^{+0.4}_{-0.6}$, by Barone-Nugent et al. (2014). Then, the virial radius is calculated by

$$r_{vir} = \left(\frac{2GM_{vir}}{\Delta_{vir}\Omega_m(z)H(z)^2} \right)^{1/3}, \quad (1)$$

where $\Delta_{vir} \approx (18\pi^2 + 60x - 32x^2)/\Omega_m(z)$ and $x = \Omega_m(z) - 1$ (Bryan & Norman 1998). The uncertainties in the estimation of virial radii are not considered here. We exclude the $z \sim 12$ data because the analysis result of Behroozi et al. (2013) does not extend to that redshift. We note that Kravtsov (2013) have conducted a similar analysis for local galaxies, and have found a linear relation between half-mass radius and virial radius over eight orders of magnitude in stellar mass. Our analysis represents the first analysis of the evolution of the relation of the galaxy and halo sizes over a wide redshift range based on the abundance matching technique.

Figure 7 shows the ratio of half-light radius to virial radius for galaxies over $z \sim 2.5-9.5$. When limited to the data of average r_e measurements, we find the ratio to be virtually constant at $3.3 \pm 0.1\%$ over the entire redshift range. The modal data of Curtis-Lake et al. (2014) give systematically higher ratios over $z \sim 5-8$, perhaps showing a slight decrease toward $z \sim 4$, but the differences from 3.3% are mostly within the $1-2\sigma$ errors. Thus, the assumption of a constant r_e/r_{vir} ratio appears to be broadly consistent with the data. Our analysis shows that the halo mass of $(0.3-1)L^*_{z=3}$ galaxies mildly decreases with redshift. This, combined with the constant r_e/r_{vir} ratio found here, results in the redshift evolution

[8] They showed the relation for $z \sim 4$ and state that it is consistent with no evolution at $z \sim 4-7$

of $1 < m < 1.5$.

According to the disk formation model by Mo et al. (1998), r_e/r_{vir} is described as:

$$\frac{r_e}{r_{vir}} = \frac{1.678}{\sqrt{2}} \left(\frac{j_d}{m_d}\lambda\right) {f_c}^{-1/2} f_R \quad (2)$$

$$\equiv \frac{1.678}{\sqrt{2}}\lambda', \quad (3)$$

for a self-gravitating disk embedded in a NFW dark matter halo, where $r_e = 1.678R_d$ (R_d is the scale length of the exponential disk), m_d and j_d are, respectively, the fractions of the mass and angular momentum within the halo belonging to the disk, λ the spin parameter of the halo, f_c a function of the halo concentration c_{vir}, and f_R a function concerning baryonic contraction. In the context of this model, our ratio (for average r_e) gives $\lambda' = 3.3\% \times \sqrt{2}/1.678 \simeq 0.028$.

Although λ and c_{vir} are well determined by N-body simulations (Vitvitska et al. 2002; Davis & Natarajan 2009; Prada et al. 2012), j_d and m_d are not reliably predicted because complicated baryonic precesses have to be considered. Since the size ratio, that is λ', is proportional to j_d/m_d while, with a fixed j_d/m_d, being dependent more weakly on m_d through f_R and essentially insensitive to j_d, we here aim to find out what value of j_d/m_d is reasonable. The shaded bands in Figure 7 are the ratios calculated from Equation (2) using the simulation results of λ by Vitvitska et al. (2002) and Davis & Natarajan (2009) and c_{vir} by Prada et al. (2012) for three j_d/m_d values over a conservative m_d range of $0.05 \leq m_d \leq 0.1$. We find that the observed size ratio is consistent with the model when $j_d \sim m_d$ is assumed.

The ratio of 3.3% is larger than that for local galaxies reported by Kravtsov (2013), 1.5%, implying that the ratio decreases from $z \sim 2.5$ to the present day. Indeed, Kravtsov (2013) have compared the local value with a theoretically plausible value for galaxies at the era of disk formation, $\simeq 3.2\%$, and attributed the lower local ratio to pseudo growth of dark matter halos since disk formation. In any case, our finding of a constant r_e/r_{vir} ratio of 3.3% over a wide redshift range of $2.5 \lesssim z \lesssim 9.5$ strongly constrains disk formation models.

3.3. *Star-formation Rate Surface Density*

The physical state of star formation of a galaxy is effectively described by the total *SFR* and the Σ_{SFR}. While the former is just the scale of star formation, the latter corresponds to the intensity of star formation and is useful for discussing the mode of star formation. We calculate the *SFR* and Σ_{SFR} for our galaxies with equations (3) from Kennicutt (1998) and (4) from Ono et al. (2013), respectively:

$$\frac{SFR}{M_\odot \mathrm{yr}^{-1}} = 1.4 \times 10^{-28} \frac{L_\nu}{\mathrm{erg\ s^{-1}\ Hz^{-1}}} \quad (4)$$

$$\Sigma_{SFR} = \frac{SFR/2}{\pi {r_e}^2}. \quad (5)$$

The weighted-log-average Σ_{SFR}s of $(0.3-1)L^*_{z=3}$ galaxies considering the uncertainty in the mass model are 4.1 $M_\odot \mathrm{yr}^{-1}\mathrm{kpc}^{-2}$ at $z \sim 6-7$ and 5.6 $M_\odot \mathrm{yr}^{-1}\mathrm{kpc}^{-2}$ at $z \sim 8$, slightly higher than 3.5 $M_\odot \mathrm{yr}^{-1}\mathrm{kpc}^{-2}$ at $z \sim 7$ and 3.2 $M_\odot \mathrm{yr}^{-1}\mathrm{kpc}^{-2}$ at $z \sim 8$ by Ono et al. (2013).

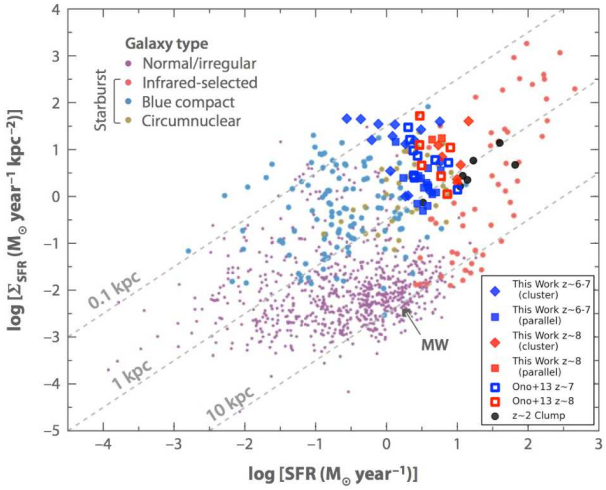

Figure 8. Distribution of our galaxies in the *SFR*–Σ_{SFR} plane, overplotted with a various types of local galaxies and star-forming clumps of $z \sim 2$ galaxies (Genzel et al. 2011). Plotted on Fig. 9 in Kennicutt & Evans (2012).

As found from Figure 4, our galaxies are forming stars with a rate of $SFR \sim 1-10\ M_\odot \mathrm{yr}^{-1}$ and with a surface intensity of $\Sigma_{SFR} \sim 1-50\ M_\odot \mathrm{yr}^{-1}\mathrm{kpc}^{-2}$. This Σ_{SFR} range is slightly wider toward higher values than reported by Ono et al. (2013) based on HUDF12, reflecting the fact that our galaxies are distributed over a wider area in the size–luminosity plane than those of Ono et al. (2013). Our sample extends especially toward smaller half-light radii.

We show in Figure 8 the distribution in the *SFR*–Σ_{SFR} plane of our galaxies and various types of local galaxies, in order to examine in what sense the state of star formation of $z \sim 6-8$ galaxies are similar or dissimilar to local ones. Comparison to normal galaxies finds that our galaxies have much higher (typically three orders of magnitude higher) Σ_{SFR}s than normal galaxies in spite of having modest *SFR*s similar to that of the Milky Way. In other words, $z \sim 6-8$ galaxies are forming stars at similar rates to local normal galaxies but in 10^3 times smaller areas.

Our galaxies are roughly comparable in Σ_{SFR} to average infrared-selected galaxies and to blue compact galaxies, while falling between these two galaxy populations in *SFR*. It is circumnuclear regions that resembles our galaxies most. Circumnuclear regions are not the whole bodies of galaxies but starbursting rings at the center of a certain type of galaxies in which gas is effectively fed along bars. This resemblance may suggest that $z \sim 6-8$ galaxies have a similar amount of cold gas of a similarly high density to that of circumnuclear regions.

Ono et al. (2013) have found that the Σ_{SFR}s of $z \sim 7-8$ galaxies are comparable to those of infrared-selected galaxies and circumnuclear regions. While we confirm this finding above, we also find that infrared-selected galaxies are scaled-up systems in terms of *SFR*.

Finally, we find that our galaxies have similar Σ_{SFR}s but slightly lower *SFR*s than star-forming clumps of $z \sim 2$ galaxies taken from Genzel et al. (2011) (black dots in Figure 8). In this sense, $z \sim 6-8$ galaxies may be considered to be scaled-down systems of clumps.

In this subsection we have neglected dust extinction.

If we use UV slope to calculate the extinction at 1600Å, A_{1600}, according to Meurer et al. (1999)'s formula, we find a median $A_{1600} = 1.2$ in our sample, corresponding to a factor 2.9 increase in *SFR* (and $\Sigma_{\rm SFR}$). Therefore, if Meurer et al. (1999)'s formula is still applicable to $z \sim 6-8$ galaxies (although they could have very different stellar populations and dust properties from local starbursts), then a significant fraction of our galaxies enter the region in the *SFR*–$\Sigma_{\rm SFR}$ plane occupied by local infrared-selected galaxies.

4. CONCLUSIONS

We have used the complete data of the Abell 2744 cluster and parallel fields taken in the HFF program to measure the intrinsic size and magnitude of 31 $z \sim 6-7$ galaxies and eight $z \sim 8$ galaxies by directly fitting light profiles of observed galaxies with lensing-distorted Sérsic profiles on the image plane with the `glafic` software. The lensing effect has been calculated using the mass map constructed by Ishigaki et al. (2015). Our sample includes a very faint galaxy with $M_{\rm UV} = -16.6$ that is detected thanks to high magnification. Combining with the HUDF12 sample of Ono et al. (2013) that is based on essentially the same method of two-dimensional Sérsic profile fitting, we now have uniform samples of 40 $z \sim 6-7$ galaxies and 14 at $z \sim 8$ galaxies with accurate size measurements. These large samples enable us to study the statistics of galaxy sizes and their dependence on other physical parameters at these high redshifts. The followings are the main results obtained in this paper.

(i) We have found that a correlation between the half-light radius and UV luminosity indeed exists, but it is not very tight. We have also found that largest ($r_{\rm e} > 0.8$ kpc) galaxies are mostly bright and red in UV color while smallest ($r_{\rm e} < 0.08$ kpc) ones mostly blue, and that galaxies with multiple cores tend to be bright.

(ii) We have compared the size–luminosity relation at $z \sim 6-8$ with those of LBGs over $2.5 \lesssim z \lesssim 9-10$ taken from the literature. The average size of bright galaxies decreases from $z \sim 2.5$ to $z \sim 7$ but the evolution slows down beyond $z \sim 7$. Irregular galaxies at $z \sim 0.5$ have a similarly steep slope of the size–luminosity relation to $z \sim 6-8$ LBGs. The average size of bright ($(0.3-1)L^{\star}_{z=3}$) galaxies scales as $(1+z)^{-m}$ with $m = 1.24 \pm 0.1$ over $2.5 \lesssim z \lesssim 12$, which is consistent with previous studies (Oesch et al. 2010; Ono et al. 2013).

(iii) We have used the abundance matching results by Behroozi et al. (2013) to find that the ratio of half-light radius to virial radius is virtually constant at $3.3 \pm 0.1\%$ over $2.5 \lesssim z \lesssim 9.5$. This constant ratio is in good agreement with the disk formation model by Mo et al. (1998) with plausible values of parameters describing the halo structure, if we take $j_{\rm d} \sim m_{\rm d}$.

(iv) The $\Sigma_{\rm SFR}$s of $z \sim 6-8$ galaxies are typically three orders of magnitude higher than those of local normal spiral galaxies. The distribution of our galaxies in the *SFR*–$\Sigma_{\rm SFR}$ plane is largely overlapped with that of circumnuclear star-forming regions in local barred galaxies, which may suggest a similarity in the environment of star formation.

This is a first report of size analysis using the data from the HFF. The complete observations of the six HFF clusters will provide us with more statistically significant samples, including very faint galaxies that have never been investigated. Size measurements for these new samples will help advance our understanding of galaxy formation and evolution through galaxy size studies, which provide complementary information to luminosity and color studies.

We would like to thank Yoshiaki Ono for his helpful comments and kindly providing with us the HUDF12 data. This work was supported in part by World Premier International Research Center Initiative (WPI Initiative), MEXT, Japan, and Grant-in-Aid for Scientific Research from the JSPS (26800093).

Facilities: HST(ACS/WFC3IR).

REFERENCES

Alavi, A., Siana, B., Richard, J., et al. 2014, ApJ, 780, 143
Atek, H., Richard, J., Kneib, J.-P., et al. 2014a, ArXiv e-prints, arXiv:1409.0512
—. 2014b, ApJ, 786, 60
Barone-Nugent, R. L., Wyithe, J. S. B., Trenti, M., et al. 2013, ArXiv e-prints, arXiv:1303.6109
Barone-Nugent, R. L., Trenti, M., Wyithe, J. S. B., et al. 2014, ArXiv e-prints, arXiv:1407.7316
Beckwith, S. V. W., Stiavelli, M., Koekemoer, A. M., et al. 2006, AJ, 132, 1729
Behroozi, P. S., Wechsler, R. H., & Conroy, C. 2013, ApJ, 770, 57
Bertin, E., & Arnouts, S. 1996, A&AS, 117, 393
Bertin, E., Mellier, Y., Radovich, M., et al. 2002, in Astronomical Society of the Pacific Conference Series, Vol. 281, Astronomical Data Analysis Software and Systems XI, ed. D. A. Bohlender, D. Durand, & T. H. Handley, 228
Bouwens, R. J., Illingworth, G. D., Blakeslee, J. P., Broadhurst, T. J., & Franx, M. 2004, ApJ, 611, L1
Bouwens, R. J., Illingworth, G. D., Oesch, P. A., et al. 2013, ArXiv e-prints, arXiv:1306.2950
Bryan, G. L., & Norman, M. L. 1998, ApJ, 495, 80
Coe, D., Bradley, L., & Zitrin, A. 2014, ArXiv e-prints, arXiv:1405.0011
Curtis-Lake, E., McLure, R. J., Dunlop, J. S., et al. 2014, ArXiv e-prints, arXiv:1409.1832
Davis, A. J., & Natarajan, P. 2009, MNRAS, 393, 1498
de Jong, R. S., & Lacey, C. 2000, ApJ, 545, 781
Dunlop, J. S., Rogers, A. B., McLure, R. J., et al. 2013, MNRAS, 432, 3520
Ellis, R. S., McLure, R. J., Dunlop, J. S., et al. 2013, ApJ, 763, L7
Ferguson, H. C., Dickinson, M., Giavalisco, M., et al. 2004, ApJ, 600, L107
Genzel, R., Newman, S., Jones, T., et al. 2011, ApJ, 733, 101
González, V., Labbé, I., Bouwens, R. J., et al. 2011, ApJ, 735, L34
Grazian, A., Castellano, M., Fontana, A., et al. 2012, A&A, 547, A51
Grogin, N. A., Kocevski, D. D., Faber, S. M., et al. 2011, ApJS, 197, 35
Guo, Y., Giavalisco, M., Ferguson, H. C., Cassata, P., & Koekemoer, A. M. 2012, ApJ, 757, 120
Hathi, N. P., Jansen, R. A., Windhorst, R. A., et al. 2008, AJ, 135, 156
Holwerda, B. W., Bouwens, R., Oesch, P., et al. 2014, ArXiv e-prints, arXiv:1406.1180
Huang, K.-H., Ferguson, H. C., Ravindranath, S., & Su, J. 2013, ApJ, 765, 68
Ishigaki, M., Kawamata, R., Ouchi, M., et al. 2015, ApJ, 799, 12
Jiang, L., Egami, E., Fan, X., et al. 2013, ApJ, 773, 153
Kennicutt, R. C., & Evans, N. J. 2012, ARA&A, 50, 531

Kennicutt, Jr., R. C. 1998, ApJ, 498, 541
Koekemoer, A. M., Faber, S. M., Ferguson, H. C., et al. 2011, ApJS, 197, 36
Koekemoer, A. M., Ellis, R. S., McLure, R. J., et al. 2013, ApJS, 209, 3
Kravtsov, A. V. 2013, ApJ, 764, L31
Laporte, N., Streblyanska, A., Clement, B., et al. 2014, A&A, 562, L8
Law, D. R., Steidel, C. C., Shapley, A. E., et al. 2012, ApJ, 745, 85
Lotz, J. M., Jonsson, P., Cox, T. J., & Primack, J. R. 2008, MNRAS, 391, 1137
Meurer, G. R., Heckman, T. M., & Calzetti, D. 1999, ApJ, 521, 64
Mo, H. J., Mao, S., & White, S. D. M. 1998, MNRAS, 295, 319
Oesch, P. A., Bouwens, R. J., Carollo, C. M., et al. 2010, ApJ, 709, L21
Oguri, M. 2010, PASJ, 62, 1017
Oke, J. B., & Gunn, J. E. 1983, ApJ, 266, 713
Ono, Y., Ouchi, M., Curtis-Lake, E., et al. 2013, ApJ, 777, 155
Peng, C. Y., Ho, L. C., Impey, C. D., & Rix, H.-W. 2002, AJ, 124, 266
—. 2010, AJ, 139, 2097
Prada, F., Klypin, A. A., Cuesta, A. J., Betancort-Rijo, J. E., & Primack, J. 2012, MNRAS, 423, 3018
Ravindranath, S., Giavalisco, M., Ferguson, H. C., et al. 2006, ApJ, 652, 963
Reddy, N. A., & Steidel, C. C. 2009, ApJ, 692, 778
Robertson, B. E., Ellis, R. S., Dunlop, J. S., et al. 2014, ApJ, 796, L27
Roche, N., Ratnatunga, K., Griffiths, R. E., Im, M., & Neuschaefer, L. 1996, MNRAS, 282, 1247
Steidel, C. C., Adelberger, K. L., Giavalisco, M., Dickinson, M., & Pettini, M. 1999, ApJ, 519, 1
Vitvitska, M., Klypin, A. A., Kravtsov, A. V., et al. 2002, ApJ, 581, 799
Zheng, W., Shu, X., Moustakas, J., et al. 2014, ArXiv e-prints, arXiv:1402.6743

APPENDIX

SUPPLEMENTAL FIGURES

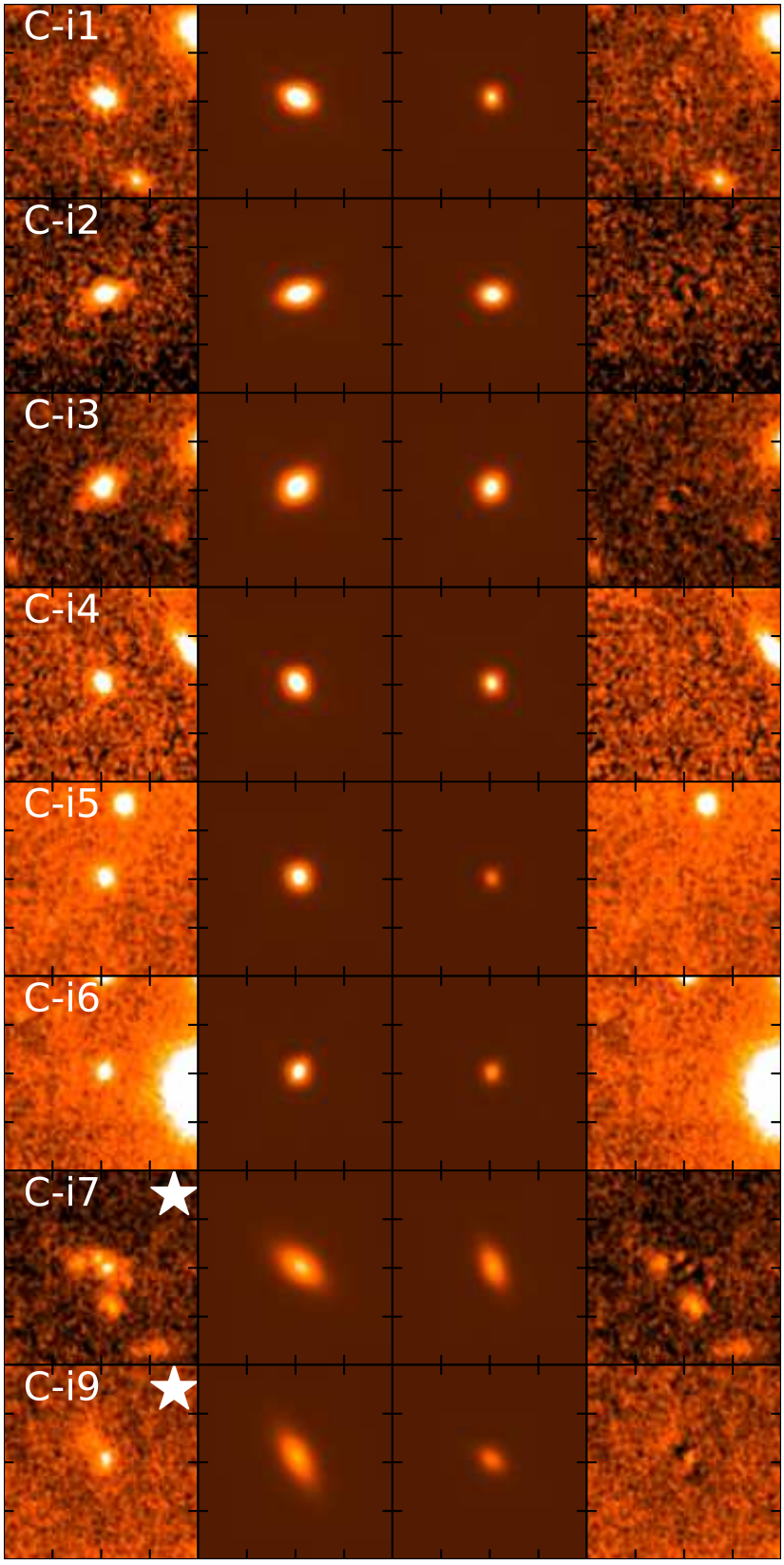

Figure 9. Fitting results for $z \sim 6-7$ galaxies in the cluster field. From left to right, $3'' \times 3''$ cut-out images, best-fit Sérsic profiles on image plane, best-fit Sérsic profiles on source plane, and residual images. Galaxies with multiple cores are marked with a star. A high resolution version of Figures 9–14 is available at `http://hikari.astron.s.u-tokyo.ac.jp/~kawamata/articles/size-abell2744/supplemental-figures`.

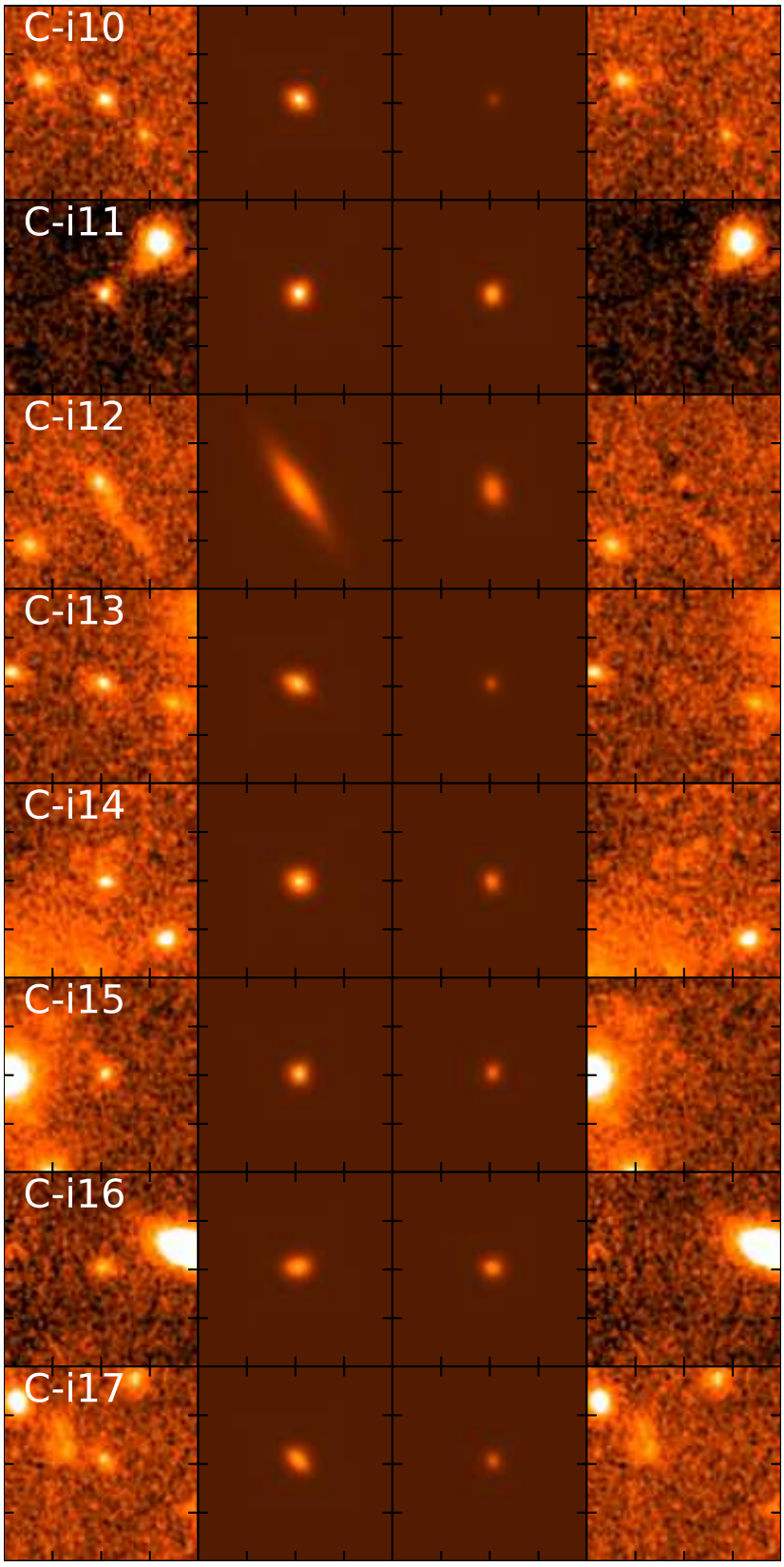

Figure 10. Continuation of Figure 9

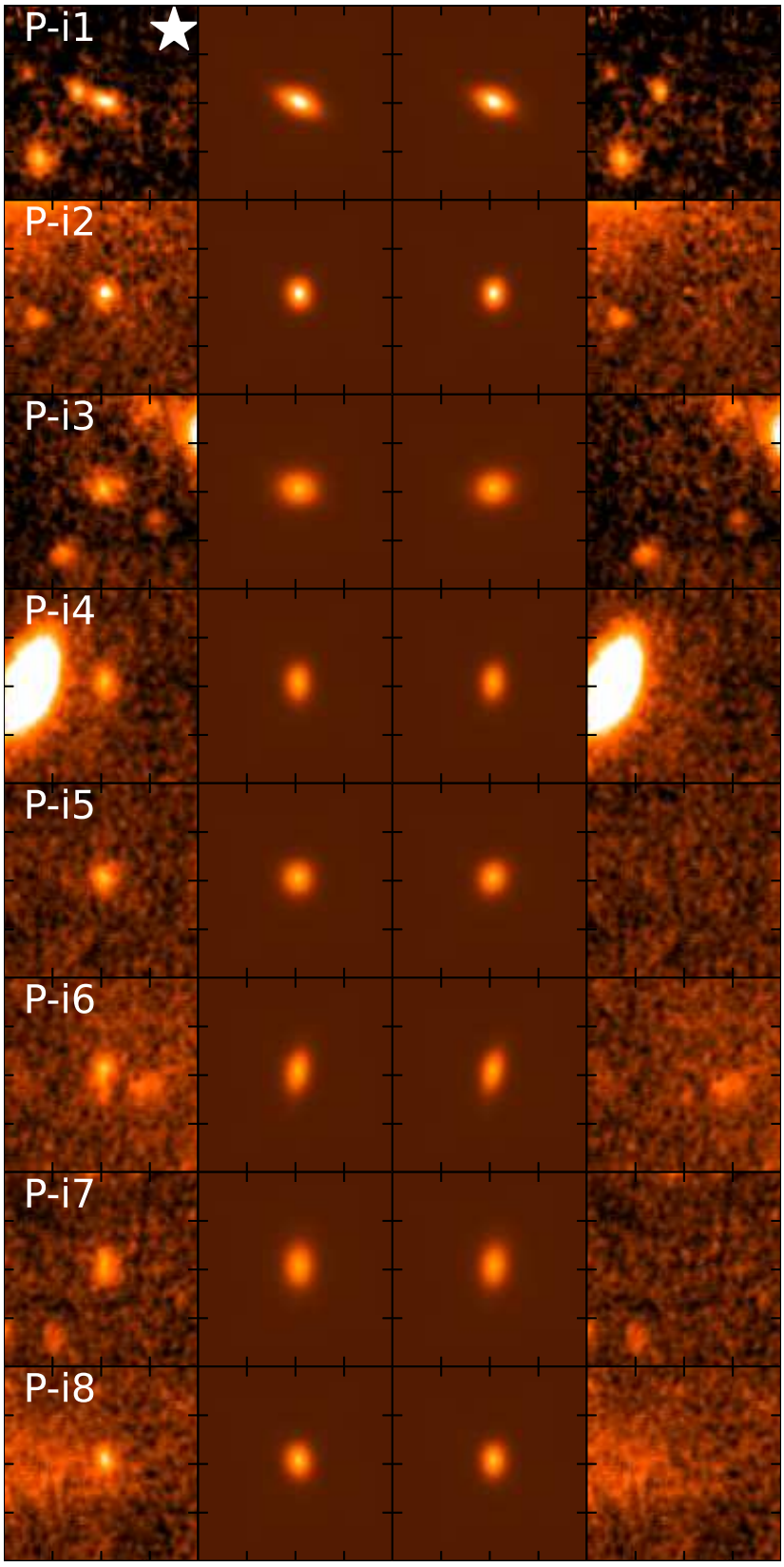

Figure 11. Same as Figure 9 but for $z \sim 6-7$ galaxies in the parallel field.

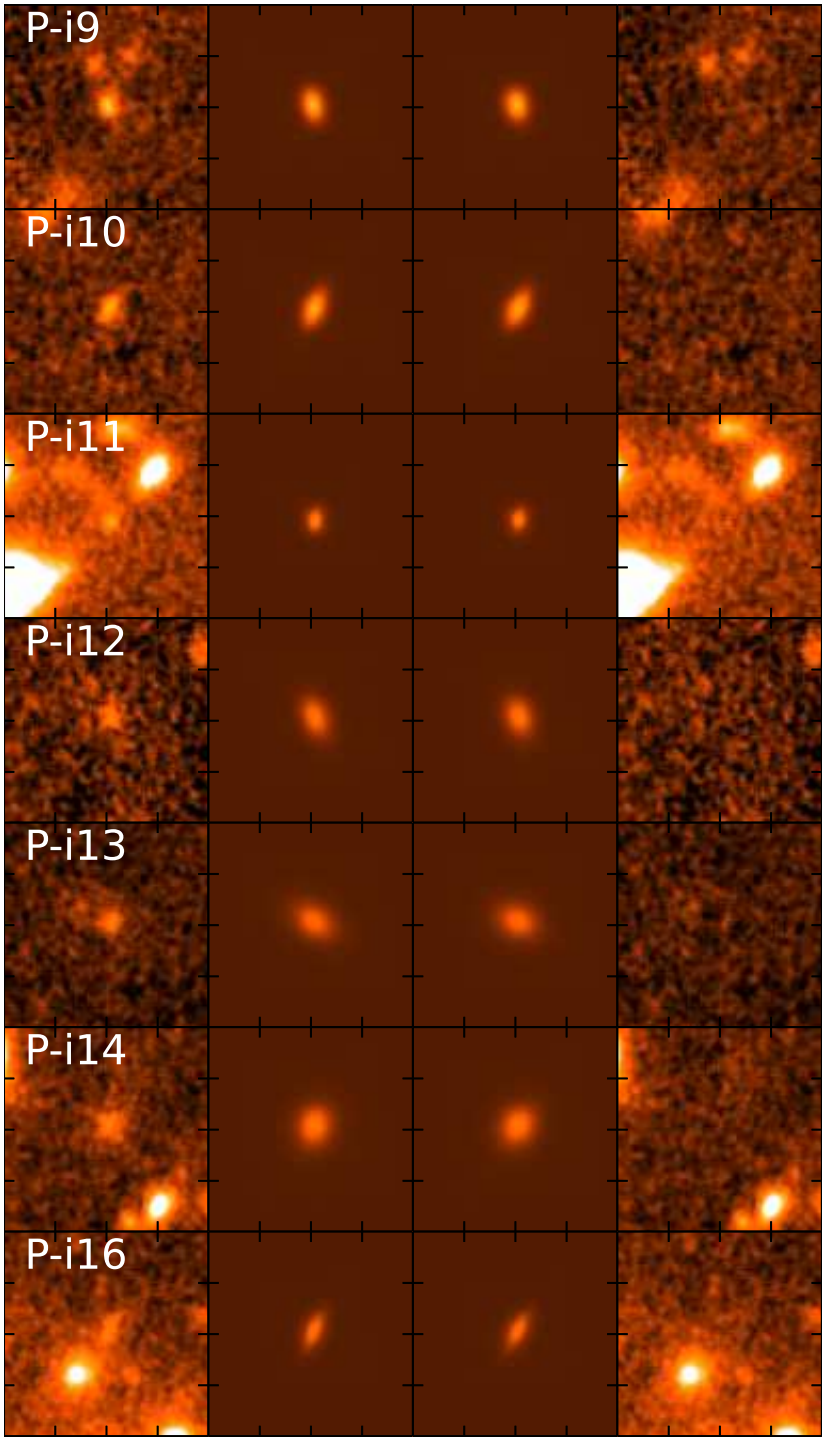

Figure 12. Continuation of Figure 11

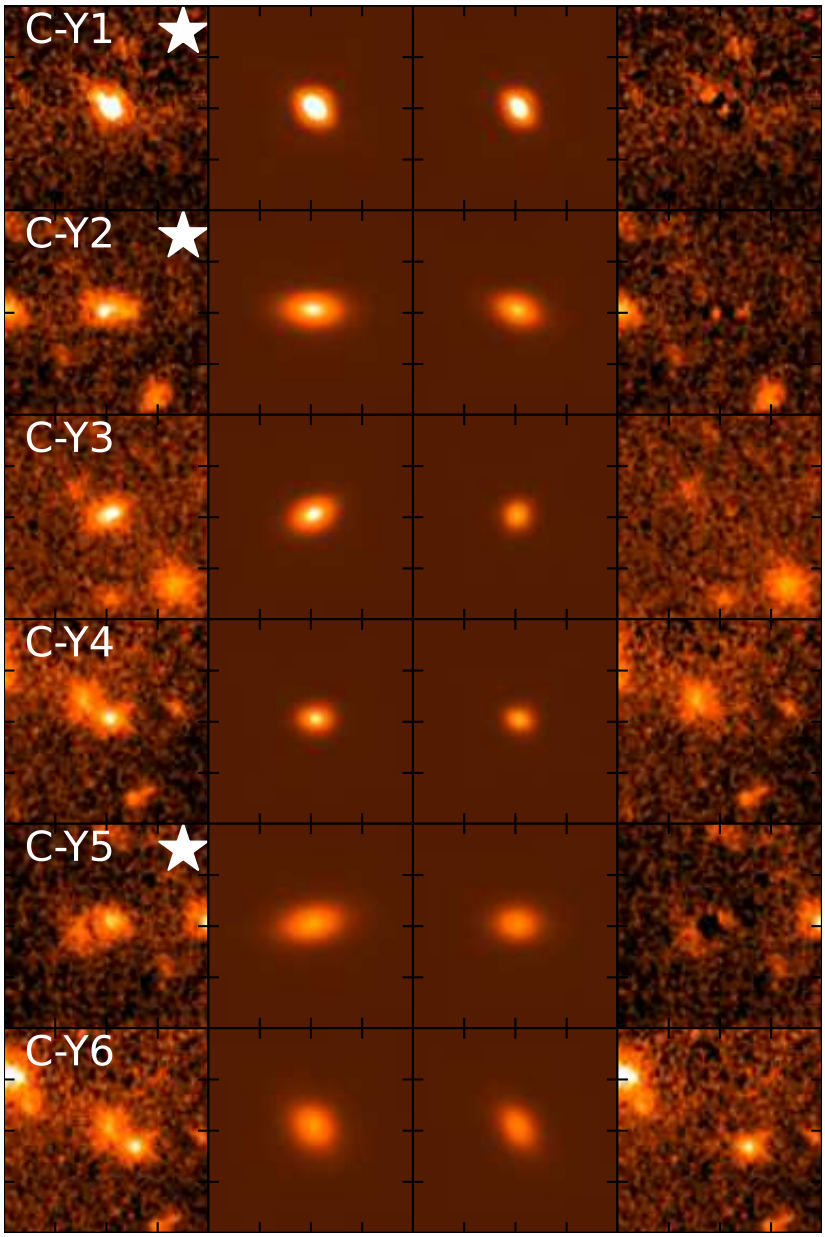

Figure 13. Same as Figure 9 but for $z \sim 8$ galaxies in the cluster field.

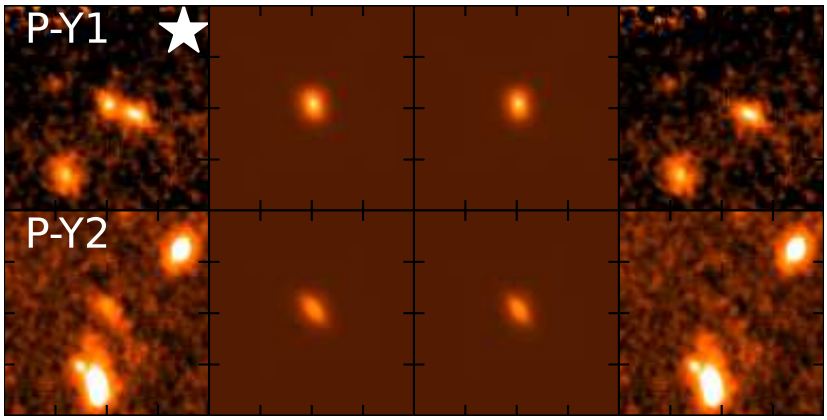

Figure 14. Same as Figure 9 but for $z \sim 8$ galaxies in the parallel field.